Chemical Science

ROYAL SOCIETY
OF CHEMISTRY

EDGE ARTICLE
Wei Han, King Lun Yeung *et al.*
Gel transformation as a general strategy for fabrication of
highly porous multiscale MOF architectures

Chemical Science

EDGE ARTICLE

Check for updates

Gel transformation as a general strategy for fabrication of highly porous multiscale MOF architectures†

Zhang Liu,[acd] Javier Lopez Navas, [b] Wei Han, [*acde] Manuel Ricardo Ibarra,[fg] Joseph Kai Cho Kwan[acd] and King Lun Yeung [*abcde]

The structure and chemistry of metal–organic frameworks or MOFs dictate their properties and functionalities. However, their architecture and form are essential for facilitating the transport of molecules, the flow of electrons, the conduction of heat, the transmission of light, and the propagation of force, which are vital in many applications. This work explores the transformation of inorganic gels into MOFs as a general strategy to construct complex porous MOF architectures at nano, micro, and millimeter length scales. MOFs can be induced to form along three different pathways governed by gel dissolution, MOF nucleation, and crystallization kinetics. Slow gel dissolution, rapid nucleation, and moderate crystal growth result in a pseudomorphic transformation (pathway 1) that preserves the original network structure and pores, while a comparably faster crystallization displays significant localized structural changes but still preserves network interconnectivity (pathway 2). MOF exfoliates from the gel surface during rapid dissolution, thus inducing nucleation in the pore liquid leading to a dense assembly of percolated MOF particles (pathway 3). Thus, the prepared MOF 3D objects and architectures can be fabricated with superb mechanical strength (>98.7 MPa), excellent permeability (>3.4 × 10^{-10} m^2), and large surface area (1100 m^2 g^{-1}) and mesopore volumes (1.1 cm^3 g^{-1}).

Introduction

Metal–organic frameworks (MOFs) represent an exciting class of reticulated, microporous materials comprising a periodic array of metal clusters and organic linkers.[1–3] MOFs can display unique and surprising interactions with matter (*i.e.*, gases, liquids, and ions) and energy (*i.e.*, light, acoustic, thermal, and mechanical).[4–7] For example, ZIF-8 has distinct network configuration, crystal symmetry, and pore topology, and displays auxetic properties, as demonstrated by the large negative compressibility after water intrusion into its superhydrophobic pores.[8,9] Many other MOFs made of different metals such as Zn, Cu, Al, Cr, *etc.* also present elastic behavior with a negative Poisson's ratio.[10–12] The fact that these materials exhibit extraordinary structural flexibility and chemical tunability has captured the imagination of scientists and industrialists alike for their potential to address some of the grand challenges the world faces in terms of the environment, energy, and health.[13–17] Indeed, the latest reported number of MOFs synthesized surpasses 80 000,[18] promising an enormous range of possible properties from these materials.

Numerous applications in catalysis, electronics, and biomedicines demand specialized architectures to facilitate transport processes, enhance material properties, and maximize functionality.[19–21] Early efforts in shaping and forming MOF materials include depositing a thin skin of MOFs on structured supports (*e.g.*, foams, honeycombs), including metals,[22–24] silica,[25–27] ceramics,[28–30] polymers,[31–36] carbon,[37–39] and graphene.[40–43] Mechanical assembly of MOFs produces freestanding monoliths,[44–47] while xerogels and dense aerogels are prepared from direct reactions of metal salts and ligands in solvents.[48–51] The latter approach is promising but has been demonstrated mainly for high-valence metals (*i.e.*, Fe, Al, Zr) and carboxylate ligands. Moreover, the network formation process (*i.e.*, gelation) is difficult as the strong affinity between metal ions and ligands favors the propagation of the framework

Division of Environment and Sustainability, The Hong Kong University of Science and Technology, Clear Water Bay, Kowloon, Hong Kong SAR, China. E-mail: kekyeung@ust.hk; keweihan@ust.hk

Department of Chemical and Biological Engineering, The Hong Kong University of Science and Technology, Clear Water Bay, Kowloon, Hong Kong SAR, China

HKUST Shenzhen Research Institute, Hi-tech Park, Shenzhen, 518057, China

HKUST Shenzhen-Hong Kong Collaborative Innovation Research Institute, Futian, Shenzhen, China

Guangzhou HKUST Fok Ying Tung Research Institute, Nansha IT Park, Guangzhou, 511458, China

Instituto de Nanociencia y Materiales de Aragón (INMA), Laboratory of Advanced Microscopies (LMA), Universidad de Zaragoza, 50018 Zaragoza, Spain

Departamento de Física de la Materia Condensada, Facultad de Ciencias, Universidad de Zaragoza, 50009 Zaragoza, Spain

† Electronic supplementary information (ESI) available: Experimental details, as well as supplementary figures and tables. See DOI: https://doi.org/10.1039/d3sc00905j

topologies rather than crosslinking the discrete nucleates into a gel network.[52] It is partly addressed by using secondary molecules to trigger the gelation and create a composite network to support the growth of MOFs.[53,54] Nevertheless, the resulting solids are often dense and have low porosity.[55] Also, a printable mixture of bentonite, copper salt, and trimesic acid with PVA binder was successfully converted to HKUST-1 using solvent and temperature to activate and control the reaction.[56] This work presents a convenient and generalized approach to constructing 3D MOF objects. It involves the assembly of the metal clusters into a skeletal gel network to create a semi-rigid, formable, viscoelastic material suitable for print extrusion. This dynamic phase-ordering process sees cluster aggregations (*i.e.*, diffusion-limited cluster aggregation (DLCA) or reaction-limited cluster aggregation (RLCA)) propagate a fractal skeletal network that traps the suspending liquid into a gel state. Then, the appropriate organic ligands are introduced to diffuse into, exchange and react with, and transform the skeletal gel network into a MOF producing a MOF solvogel. Control over the transformation pathways is essential as it dictates the final properties of the material. It requires judiciously managing the rates of network dissolution, seed nucleation, and MOF crystallization to attain a high-fidelity, nanoscale replication of the gel network by a pseudomorphic transformation route to create MOF gels that faithfully reproduce the network structure at the nano- and micron-scales, thus preserving the pore characteristics and interconnectivity necessary for producing high porosity materials. Besides pseudomorphic transformation pathway 1, as exemplified by the conversion of zinc gel to ZIF-8 and MOF-5, the study also observed two other transformation pathways (*i.e.*, 2 and 3). Indeed, copper gel can be transformed into HKUST-1 along all three pathways by adjusting the synthesis conditions. Nonetheless, twelve MOFs were successfully fabricated into 3D objects from Al, Co, Cu, Eu, Fe, Ni, and Zn gels by molding and 3D-printing processes. Their transformation to solid MOFs produces ultralow density materials (≤ 0.12 g cm^{-3}) with high mesoporosity (≥ 0.8 cm^3 g^{-1}) and permeability ($> 3.4 \times 10^{-10}$ m^2) and enhanced strength (> 42.5 MPa). In addition, 3D-printing appropriate architectures can produce stronger materials (> 98.7 MPa) making them suitable for various applications, particularly for pollution treatment and water decontamination.[57–61]

Results and discussion

Gelation of metal precursors and transformation into MOFs

The fabrication of MOF superstructures (*e.g.*, 3D objects and architectures) begins with preparing the metal precursor sol, as illustrated in Fig. 1a(i), which involves protonation of the epoxide followed by a ring-opening process to react with the metal cations forming metal hydroxy and oxo-hydroxy species[62–64] that polymerize into a sol–gel network (Fig. 1a(ii)). Subsequently, the organic ligand is introduced (Fig. 1a(iii)) to diffuse into, react with, and transform the precursor gel network into MOFs (Fig. 1a(iv)). Finally, a MOF aerogel (Fig. 1a(v)) with hierarchical macro-/meso-/micropores is

obtained following solvent removal by a supercritical extraction and drying process.

Zn-based MOFs that have different micropore topologies, ZIF-8 with imidazolate (*i.e.*, Hmim) ligands and MOF-5 with terephthalate (*i.e.*, H$_2$BDC) ligands, were selected as examples. Fig. 1b shows the zinc precursor alcogel prepared from a mixture of zinc nitrate hexahydrate, zinc chloride, polyacrylic acid (PAA), and propylene oxide in ethanol. The protonation of propylene oxide (PO) increases the pH of the zinc solution, and PAA was added to buffer the reaction and complex with the zinc ions to control nucleation and facilitate sol–gel formation (Fig. 1c). The reaction proceeds rapidly, and the gel network is formed within 11 min (Fig. 1d and e), and the gelation is complete in 24 min (Fig. 1f) to yield stable porous gel networks (Fig. 1g) *via* spinodal decomposition.[65–67] The high-resolution transmission electron microscopy (HRTEM) image in Fig. 1g shows the gel consists of layered Zn$_5$(OH)$_8$(NO$_3$)$_2 \cdot$2H$_2$O of less than 5 nm size. PAA also increases steric hindrance, tunes the sol particle size, decreases syneresis, and prevents shrinkage of the prepared gel (Table S1†). However, high PAA concentrations (*e.g.*, >8 wt%) slow gelation as it inhibits pH increase, thus impeding nucleation and growth. Moreover, PAA modulates the rheology of the precursor gel for molding and 3D printing purposes.

Molecules can diffuse through the molded cylindrical Zn wet gel (*i.e.*, 6 mm diameter, 6.6 mm length), as illustrated in Fig. S1† for toluene ($M_w = 92.1$ g mol^{-1}) and Sudan Red ($M_w = 408.5$ g mol^{-1}). The measured diffusivities of toluene and Sudan Red were 5.94×10^{-7} cm^2 s^{-1} and 1.57×10^{-8} cm^2 s^{-1}, respectively. Thus, Hmim ($M_w = 82.1$ g mol^{-1}) and H$_2$BDC ($M_w = 166.3$ g mol^{-1}) should readily diffuse through the wet gel to react with and transform the gel network into ZIF-8 (Fig. 1h) and MOF-5 (Fig. 1i) within 24 h. Indeed, the substitutions of Hmim and H$_2$BDC for the NO$_3^-$ and OH$^-$ anions of the Zn$_5$(OH)$_8$(NO$_3$)$_2 \cdot$2H$_2$O gel network can be monitored by FTIR spectroscopy (Fig. 1j). The gel's broad Zn–O peak at 400–580 cm^{-1} disappeared with time, followed by the appearance of a ν Zn–N peak (*i.e.*, at 421 cm^{-1}) from the ZnN$_4$ clusters of ZIF-8 and a narrow ν Zn–O peak (*i.e.*, at 517 cm^{-1}) from the Zn$_4$O groups of MOF-5 along with the in-plane and out-of-plane bending of the imidazole ring and benzene ring corresponding to the Hmim and H$_2$BDC ligands in the FTIR spectra (Table S2†).[68,69] Moreover, the powder X-ray diffraction (PXRD) of the aerogel samples confirms the complete conversion to crystallized ZIF-8 and MOF-5 (Fig. 1k).[3,8]

Structural and textural changes after MOF transformation

The Zn gel network can be deduced from the image of the Zn precursor aerogel, which possesses a continuous and interwoven network of intergrown 37 ± 9 nm particles (Fig. 2a). Its transformation into crystalline ZIF-8 (Fig. 2b) and MOF-5 (Fig. 2c) slightly increases the particle sizes to 38 ± 11 nm and 41 ± 12 nm, respectively, and is accompanied by a coarsening of particle morphology and pore channels as shown in the figure insets. A focused Ga$^+$ ion beam slices the aerogel sample to reveal its interior (Fig. 2d), and after coating the
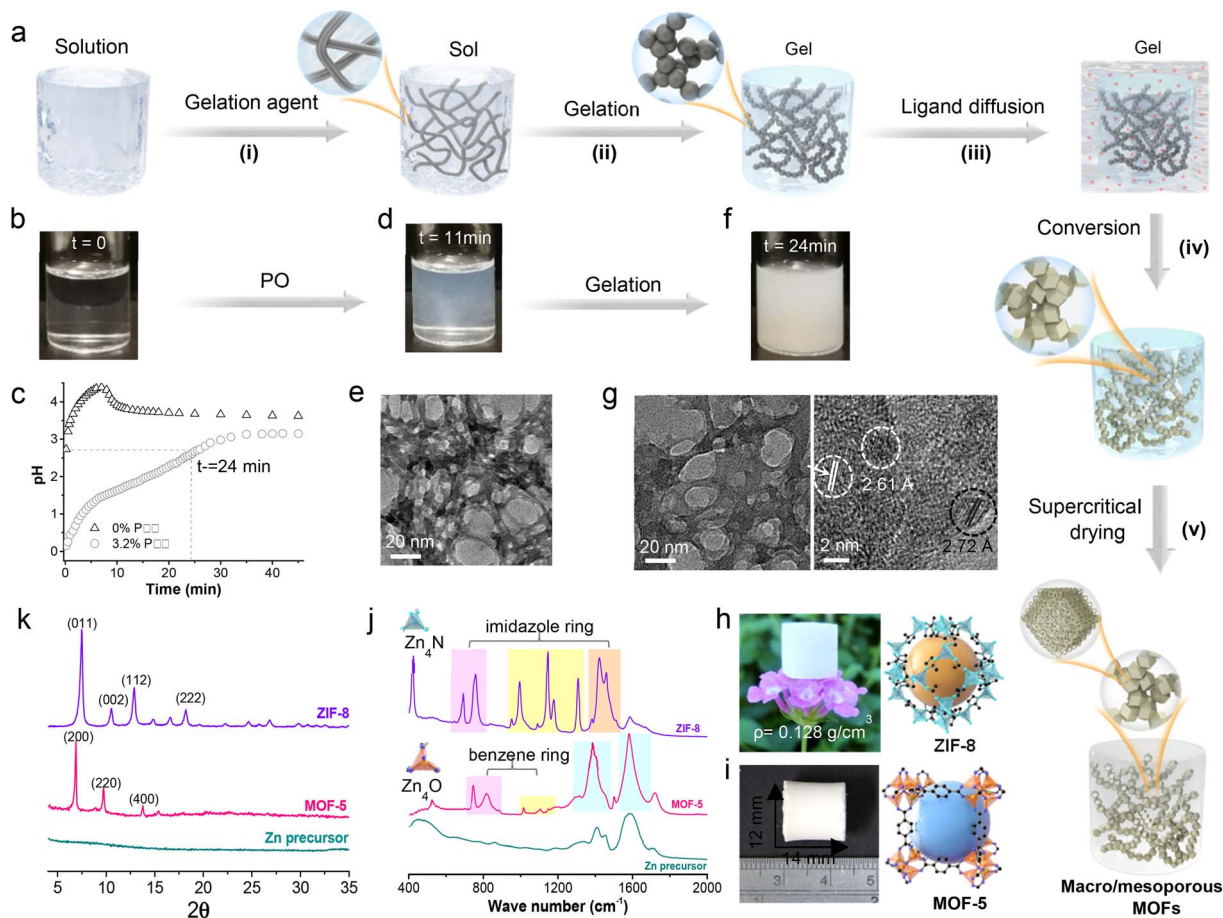
Fig. 1 Transformation route from metal precursor gels to MOF aerogels. Schematic representation of the synthesis of the macro-/meso-/microporous MOF aerogel *via* transformation of a metal precursor gel (a), sol–gel process of the Zn precursor at time zero (b), 11 min (d), and 24 min (f), and the accompanying pH during the sol–gel process (c). The TEM image of Zn sol at a time of 11 min (e) and HRTEM image at 24 min (g) correspond to samples shown in (d) and (f). Digital photos of ZIF-8 (h) and MOF-5 (i) aerogels and their FTIR (j) and XRD patterns (k). Note: ZIF-8 and MOF-5 XRD patterns can be found in literature reports.[8,69]

section with sputtered Pt (Fig. 2e), a 2D SEM image is obtained at a resolution of 5 nm per pixel. Thus, acquiring serial 2D images allows reconstruction of the 3D volume to reveal the samples' skeletal structure and pore network (Fig. 2f–h and Movies S1–S3†).[70] The converted ZIF-8 and MOF-5 largely inherited the parent skeletal network with chord length distributions shown in Fig. 2i–k, displaying trailing behavior from length expansion. This implies that MOF conversion involves a partial dissolution of the gel, contributing to a coarsening of the pore channel and the emergence of micropores attributed to the crystallized MOFs. Nevertheless, the gel and pore networks were faithfully replicated in a pseudomorphic transformation process.

The mechanical, thermal, textural, and transport properties of the samples were characterized. The Zn precursor aerogel exhibited a linear compressive deformation at low strain, indicating a relatively soft skeletal network that can flex under compression (Fig. S2†). The conversion into MOFs strengthens the material, with the ZIF-8 and MOF-5 aerogels having Young's moduli of 68.4 MPa and 42.5 MPa, respectively, comparable to those of silica aerogels.[71,72] Both MOF aerogels exhibit a strong

plastic strain–stress behavior punctuated by compaction stages. The measured thermal conductivity of a ZIF-8 aerogel was 0.031 W m^{-1} K^{-1} and is consistent with aerogel materials.[73] The N$_2$ adsorption–desorption isotherms in Fig. 3a show that the zinc precursor and MOF aerogels display type H1 hysteresis at a relatively high-pressure range. The steep rise in the isotherm at low P/P_0 for the MOF aerogels indicates nitrogen uptake into the micropores. The ZIF-8 and MOF-5 aerogels have micropores of 0.71 ± 0.06 nm and 0.80 ± 0.15 nm that are consistent with literature reports,[74,75] and are responsible for their large specific surface areas of 1312 m^2 g^{-1} and 1456 m^2 g^{-1}, compared to reported values of 700–1100 m^2 g^{-1} for ZIF-8 and MOF-5 nanoparticles prepared by solution mediated precipitation.[74,76,77] According to Barrett–Joyner–Halenda (BJH), the mean mesopore diameter of the Zn precursor is 29.5 ± 12.4 nm, and it is 35.1 ± 13.5 nm and 43.2 ± 16.6 nm for the ZIF-8 and MOF-5 aerogels, respectively, and these values are consistent with chord lengths derived from SEM tomography analysis (Fig. 2j and k), confirming that the mesopore network remains relatively intact during the gel network's transformation into MOFs.
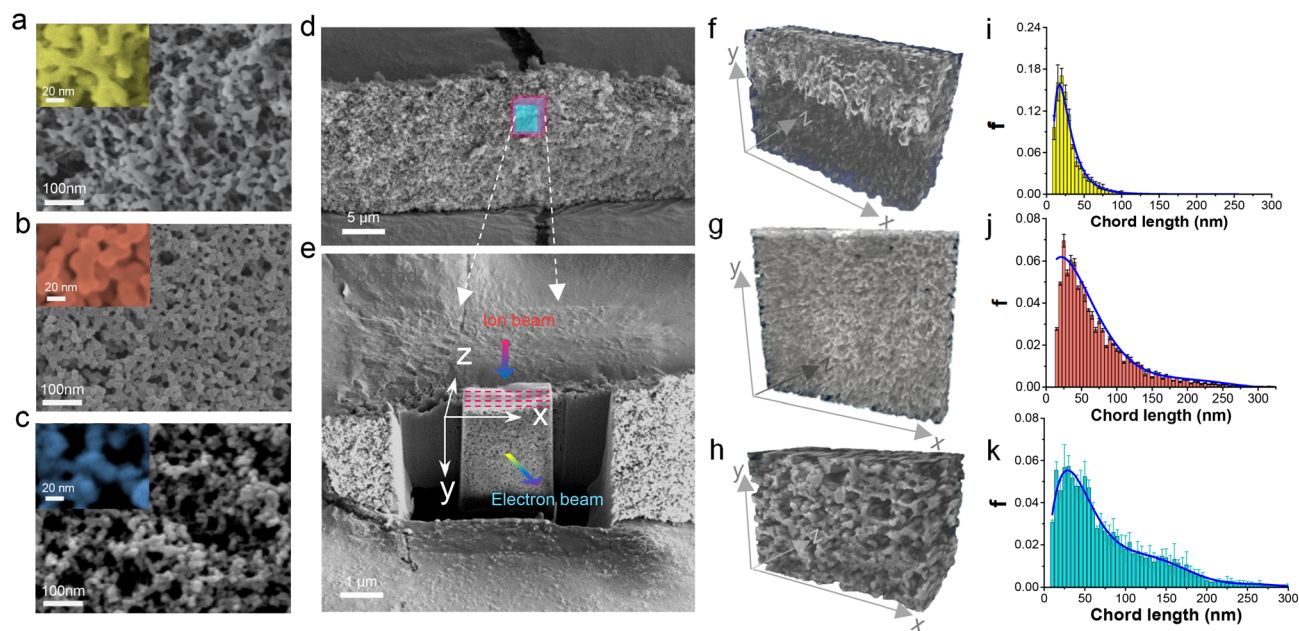
Fig. 2 Micromorphological changes during Zn precursor gel transformation to ZIF-8 and MOF-5. SEM images of the Zn precursor (a), ZIF-8 (b), and MOF-5 (c) aerogels showing highly crosslinked network structures, FIB-SEM dual beam analyses of the ZIF-8 aerogel (d and e), and the 3D reconstructed images and chord length distribution of the Zn precursor (f and i), ZIF-8 (g and j), and MOF-5 (h and k) aerogels, showing changes in their 3D micromorphology and pore interconnectivity.
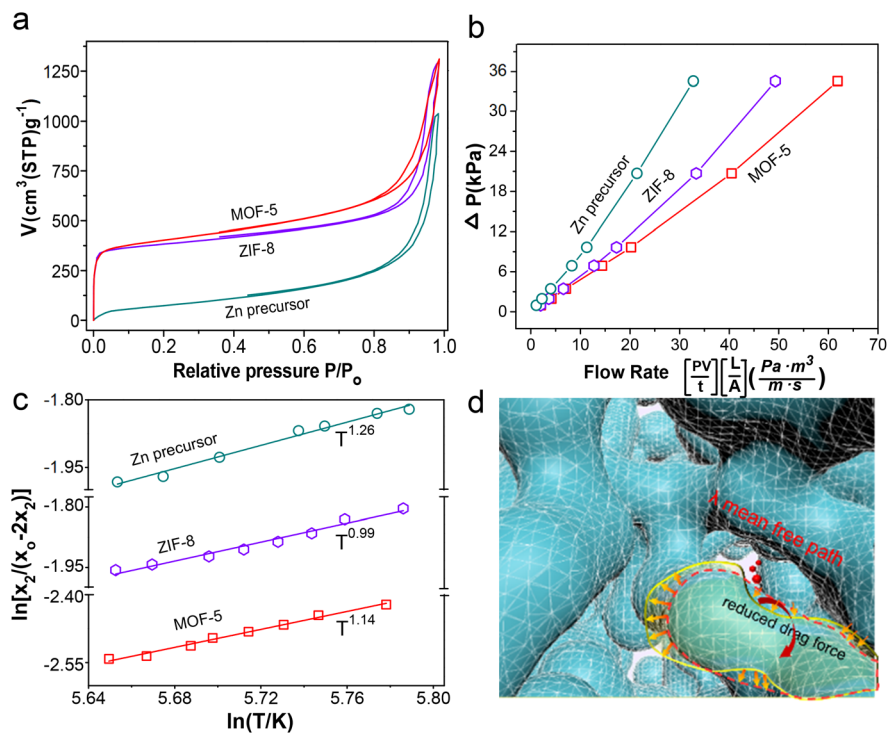

Fig. 3 Nitrogen sorption isotherms (a), oxygen permeation and diffusion (b and c) in the Zn precursor, ZIF-8 and MOF-5 aerogels, and schematic drawing (d) illustrating how MOF crystallization with substantial narrowing of "necks" contributes to a shift towards a slip flow regime.

Moreover, unlike conventional MOF monoliths, the ZIF-8 and MOF-5 aerogels prepared by the gel transformation route have very low density (*i.e.*, 0.128 g cm^{-3} and 0.157 g cm^{-3} for ZIF-8 and MOF-5, respectively) with large through-porosities (Table S3†). Oxygen permeation and diffusion through the aerogels were measured in permeation and Wicke–Kallenbach

(W–K) cells to investigate the transport behaviors of small gas molecules. The low pressure drops across the thick aerogel monolith (*i.e.*, 9 mm) attest to these materials' high permeability (Fig. 3b). It is also clear from Fig. 3c that oxygen diffusion displays $T^{1.26}$, $T^{0.99}$, and $T^{1.14}$ temperature dependency for the zinc precursor, ZIF-8, and MOF-5 aerogels, respectively. The oxygen diffusion in these materials is in the transition region between Knudsen ($T^{0.5}$) and bulk ($T^{1.5}$) diffusion. Flows through the interparticle mesopores have Knudsen numbers of 2.21 for the Zn precursor, and 1.84 and 1.49 for the ZIF-8 and MOF-5 aerogels, corresponding to the transition flow regime between slip flow ($K_n = 0.1$) and free-molecule flow ($K_n = 10$).[78] The calculated diffusivities are 5.8×10^{-6} m^2 s^{-1} for the ZIF-8 and 9.0×10^{-6} m^2 s^{-1} for the MOF-5 aerogel. At the same time, the shift of the Knudsen value towards slip flow suggests thinning of the "necks" region of the skeletal networks[79] during the transformation into MOFs (Fig. 3d), resulting in coarser interparticle pores. The crystallization of ZIF-8 and MOF-5 introduces intraparticle micropores with Knudsen numbers of 91.0 and 80.5, respectively.

Transformation kinetics and pathways

The transformation of the gel network into crystalline MOFs is further investigated on thin gel slices by X-ray diffraction (XRD),

with each synthesis yielding pure ZIF-8 (Fig. S3†). Fig. 4a presents the transient diffraction map showing the intensity variation of ZIF-8 (011), (002), (112), and (222) peaks with crystallization time and temperature. The figure insets are representative ZIF-8 particle morphologies obtained at different temperatures. At 20 °C, the diffraction peaks are weak and broad, and the (002) and (222) diffractions are faint, indicating that these crystal facets are poorly formed, which is consistent with the inset image. In contrast, rhombic dodecahedron particles associated with fully crystallized ZIF-8 are prevalent in samples crystallized at 80 °C. The crystallization curves in Fig. 4b were constructed from the most intense (011) diffraction peak (Fig. S3†). The (011) diffraction was detectable after a 120 s induction time for samples prepared at 20 °C and 40 °C, and above these temperatures, the induction time is less than 60 s. A nonlinear least-squares fit of Fig. 4b data to Gualtieri's equation yielded the nucleation probability curves in Fig. 4c and a set of kinetic parameters listed in Table S4.†

The sharp rise of α in Fig. 4b at 100, 35, 20, and 16 min coincides with the peaks of the nucleation probability curves (Fig. 4c), showing nucleation is most likely to occur at 81.3, 49.1, 25.4, and 17.7 min as temperature increases from 20 to 80 °C. It is followed by a more gradual increase of α as the nuclei grew into larger ZIF-8 crystals. The excellent linear fit of the Sharp–Hock (SH) plots (Fig. S4†) indicates that the transformation of
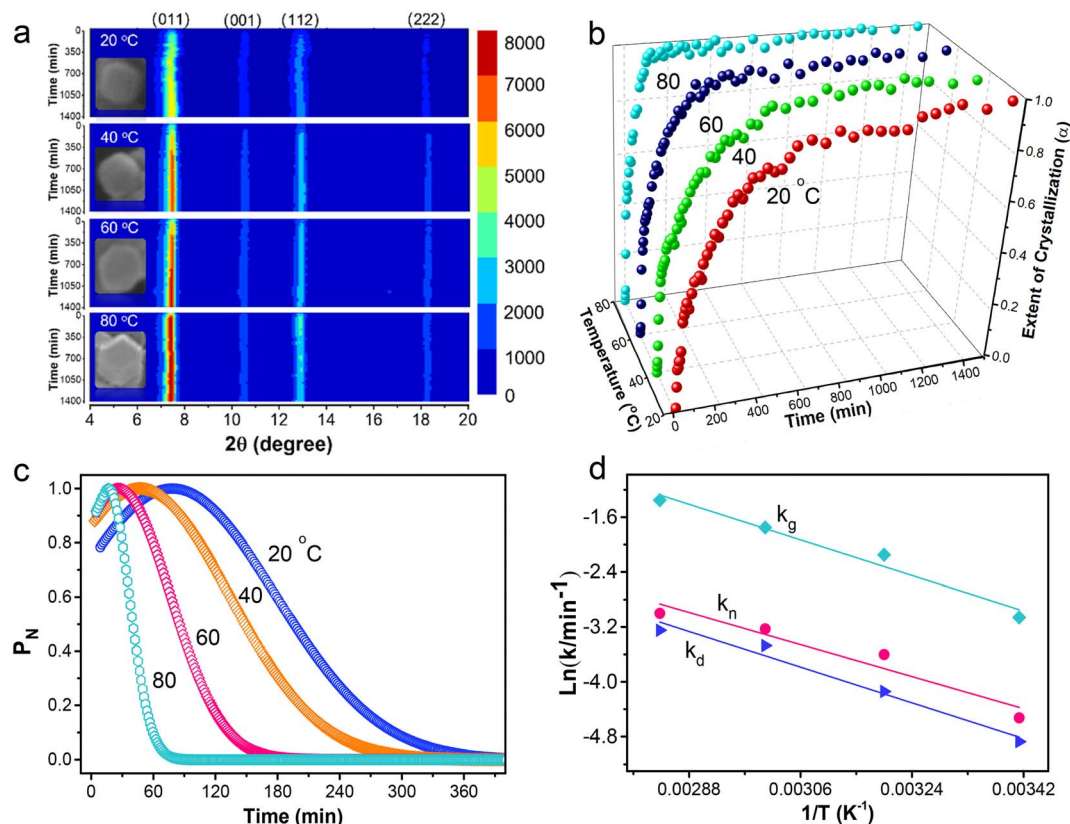

Fig. 4 Transformation kinetics of ZIF-8 from the Zn precursor gel at different temperatures. Crystallization map of ZIF-8 with time (a), extent of crystallization of ZIF-8 from the [011] characteristic diffraction peak (b), nucleation probability curves of ZIF-8 gel at temperatures of 20, 40, 60, and 80 °C (c), and Arrhenius plots for temperature dependent rate constants of dissolution (k_d), nucleation (k_n) and growth (k_g) obtained from the Gualtieri model for ZIF-8 gel transformation (d).

the gel network into intergrown ZIF-8 crystals can be described by the Avrami–Erofe'ev equation with isotropic growth behavior, suggesting that the crystallization mechanism of the gel into ZIF-8 remains unchanged.[31] Moreover, the Avrami exponent, n, determined from the SH plots, ranges from 0.4 to 0.7 (Table S5†), indicating near-instantaneous nucleation and rapid growth.[80] Thus, the transformation is diffusion controlled. According to SH analysis, the activation energy (E_a) of the entire transformation process is 22.4 kJ mol^{-1}.

Gel dissolution occurred during the transformation process and was measured in a separate experiment (Fig. S5a†). The data fit a first-order rate law (Table S6†) and indicate an activation energy (E_d) of 17.3 kJ mol^{-1}. The variance of the nucleation probability curves (b) provides an insight into the nucleation process with $b \leq 15$ indicating a mostly heterogeneous nucleation process while $b > 20$ suggests an autocatalytic nucleation,[81] wherein rapid Hmim complexation with zinc creates embryonic nuclei on the surface and bulk of the thin gel network, seeding the formation, growth, and crystallization of ZIF-8. Fig. 4d shows the nucleation (k_n) is slower than the crystal growth (k_g) during the gel transformation into ZIF-8, and the nucleation displays a strong correlation with gel dissolution (Fig. S5b†). The activation energy for the nucleation process (E_n) is 20.8 kJ mol^{-1} and the crystal growth (E_g) is 22.1 kJ mol^{-1}. These values are lower than the 69.0–71.8 kJ mol^{-1} reported for typical ZIF-8 synthesis.[82] Thus, it is easier to convert precursor gel into ZIF-8 and the transformation can proceed under mild conditions. Indeed, the same approach converts Zn precursor gels into MOF-5, ZIF-7, ZIF-90, IRMOF-3, and MOF-74(Zn) aerogels (Fig. S6 and Tables S7 and S8†). Similarly, HKUST-1, MOF-74(Ni), NH$_2$-MIL-53, MIL-101(Fe), and ZIF-67 aerogels were prepared from the corresponding copper, nickel, aluminum, iron, and cobalt precursor gels at mild temperatures.

Three transformation pathways were identified in the study. ZIF-8 follows the pseudomorphic transformation pathway 1 in Fig. 5a via an interface-coupled dissolution–precipitation (ICDP) process commonly used to describe many natural phenomena, such as mineral metamorphism and metasomatism.[83] It is also believed to be responsible for silica replication[84] and ordered zeolite arrays' formation.[85] The slow gel network dissolution and rapid nucleation at low temperatures favor ICDP resulting in the pseudomorphic replication of the gel network in the ZIF-8 and MOF-5 aerogels (Fig. 2). MOF conversion along transformation pathway 1 generally preserves the structure of the original gel network. Pathway 2 illustrated in Fig. 5b occurs when conversion is conducted at higher temperatures and the faster gel dissolution and crystallization (Fig. S5a†) result in poorer replication, as observed for ZIF-8, MOF-5, ZIF-67, and ZIF-90 aerogels prepared above 60 °C (Fig. S7a–d†). The transformation along pathway 2 preserves the network interconnectivity but displays considerable change in the local network morphology and structure, as a large fully crystallized MOF emerges.

The third transformation pathway described in Fig. 5c occurs when the gel network's dissolution is fast, super-saturating the pore liquid with metal cations and resulting in

the MOF's nucleation and growth in the pore liquid. The MOF crystals assemble via percolation and exhibit poorer network interconnectivity and weaker strength. This can be seen from the transformation of the copper precursor gel (Fig. S8a†) by trimesic acid (TMA) into HKUST-1 (Fig. S8b†). The reaction is fast, and full conversion is completed within 30 min. HKUST-1 is the only reaction product, as indicated by X-ray diffraction in Fig. S9a.† The particle size coarsened as HKUST-1 nucleates and grows in the pore solution resulting in a significant change in the size distribution (Fig. S10a†). Moreover, the corresponding nonlinear least-squares fit of the crystallization data to Gualtieri's equation (Fig. S9b†) and the kinetic parameters listed in Table S9† indicates fast dissolution of the copper gel network (Table S10†), while slow nucleation and fast crystal growth result in large, discrete HKUST-1 crystals (Fig. S8b†). MOF-74 (Zn, Ni) and MIL-101-Fe also transformed along pathway 3 (Fig. S7e–h†). It is possible to alter the HKUST-1 conversion from pathway 3 to pathway 2 by adding a higher concentration of trimesic acid solution (hi-TMA) to slow the crystallization of HKUST and allow the gradual growth of the crystals (Fig. S8c†), which is confirmed by XRD (Fig. S9c†) and particle size distribution (Fig. S10b†). Nucleation occurs early in the conversion, as shown in the Gualtieri plot of Fig. S9d,† with a similarly broad variance b (>15) characteristic of heterogeneous nucleation. The HKUST nuclei cladded the precursor gel's surface and slowed the diffusion of trimesic acid into the skeletal gel network, thus slowing the crystallization. However, the gel network dissolution remains fast (Fig. S11†), resulting in local structural changes, as observed in Fig. S8c.† Also, homogeneous nucleation in pore liquid cannot be completely excluded and could explain the presence of large octahedral HKUST crystals in Fig. S8c.† Introducing sodium formate slows the dissolution of the copper gel network (Fig. S11†) and inhibits the growth of HKUST-1 (Fig. S8d and S10c†), forcing the conversion along transformation pathway 1 (Fig. 5a). Formate complexes with copper, preventing the rapid dissolution of the gel network (Fig. S11†) and sequestering dissolved copper cations in the pore liquid, and thus, inhibiting homogeneous nucleation. Indeed, the particle size distributions remain relatively unchanged throughout the reaction (Fig. S10c†). The addition of sodium formate did not cause crystallization into a new phase, and HKUST-1 is the only product of the reaction with trimesic acid (Fig. S9e†). The Gualtieri plot of Fig. S9f† fits a broader nucleation probability curve with variance b, having a value of around 15 for heterogeneous nucleation. A fast nucleation rate and slow crystallization will lead to small crystals, thus avoiding the formation of large crystals that could disrupt the network structure.[84] The HKUST-1 examples demonstrate how the transformation pathways can be manipulated by adjusting the rates of gel dissolution, seed nucleation, and MOF crystallization to attain the desired material structure.

3D printing gels for fabricating porous MOF architectures

Besides solid objects, films, and membranes, this synthesis approach can be used to fabricate complex 3D architectures.

Fig. 5 Transformation pathways from the metal precursor alcogel to the MOF aerogel. Pathway 1 (a) or pseudomorphic transformation with a high degree of replication of the network and pore structures occurs under conditions of slow gel network dissolution, rapid nucleation, and moderate crystallization rate. Pathway 2 (b) preserves the overall network interconnectivity and occurs under moderate gel dissolution rate and slow nucleation. Pathway 3 (c) takes place under rapid gel network dissolution initiating nucleation and crystallization in the pore fluid to fill the pore spaces with discrete MOF particles.

The precursor gels can be made printable by adjusting their rheological properties with the addition of PAA (Fig. S12†). Gels with viscosities between 0.8 and 5 kPa s at a shear rate of 0.2 s^{-1} (Fig. 6a) are suitable for 3D printing, as shown in Fig. 6b. They were printed by a laboratory-designed and built 3D printer equipped with an advanced extrusion nozzle for printing precursor gels with linewidth as narrow as 200 μm (Fig. S13†). Fig. 6b presents a schematic drawing of the printing process and the two-layer 90° rectangular grid test pattern (i.e., 17 mm sides and 1.3 mm height). The Al, Zn, Eu, Fe, Ni, and Co precursor gels shown in the figure were printed at an extrusion tip movement of 2 mm s^{-1} and gel extrusion rate of 1.57 mm^3 s^{-1} to produce thin continuous printed lines of 726 ± 86 μm. Fig. 6b shows the translucent aluminum gel transformed into yellow NH$_2$-MIL-53 and white zinc gel into yellow ZIF-90, while the white europium gel converts into deep red luminescent EuBDC MOF that fluoresces under UV$_{256}$. The brown iron gel successfully converts to orange MIL-101 (Fe), the green nickel gel changes into yellow MOF-74 (Ni), and the brown cobalt gel produces deep purple ZIF-67.

Fig. 6c reports the precursor and MOF gels' storage modulus (G') measured by the oscillation stress sweep test (Fig. S14†). The measurements indicate a change in the elasticity following MOF transformation. Nevertheless, these viscoelastic gels are stable and can withstand external stresses. Indeed, their linear viscoelastic region (LVR) falls within 10% strain, further indicating that the gel network can resist deformation during

print extrusion, allowing precision printing with good reproducibility. Crystallization of the MOF alters the skeletal gel network and its viscoelastic properties, as shown in Fig. S14.† A decrease in G' is understandable as the transformation process will introduce defects in the skeletal network, with the largest drop recorded for the MOFs crystallized along pathway 3 (i.e., NH$_2$-MIL-53 (Al), MOF-74 (Ni), and MIL-101 (Fe)), where it sustained the most damage from rapid gel dissolution and percolating MOF particles crystallized from the pore liquid. As exemplified by MOF-5, ZIF-8, and HKUST-1 (hi-TMA), pseudomorphic transformation shows the smallest decrease in G' compared to the parent precursor gel (Fig. 6c).

Ten layers of 90° rectangular grid were printed from zinc (Fig. 6d) and copper (Fig. 6f) gels. Each 3D-printed object measures 17 mm along each side and is 6.5 mm tall. Each layer comprises twelve lines of 650 ± 36 mm diameter (d), and the distance between centerlines (l) is 1.5 mm. It took 12 min to print each sample at a printing speed of 3 mm s^{-1}. The corresponding gel networks were inspected by SEM and presented in the figures, following solvent exchange, supercritical extraction, and supercritical drying to preserve the original gel structure. The translucent zinc gel turns white following its transformation to ZIF-8 after immersing in 20 ml of 0.3 M Hmim in methanol for 120 min at room temperature (Fig. 6e). The SEM image shows the crystallization of ZIF-8 follows pathway 1, preserving the general network structure and pore interconnectivity. ZIF-8's characteristic rhombic dodecahedron

Fig. 6 Rheology, 3D printing, and mechanical strength of the metal precursor and converted MOF gels. Viscosity of various metal gels (a) and printability window (a, inset), 3D printing of metal gels and their conversion into the MOF test pattern (b), storage modulus of metal gels and their corresponding MOF gels as a function of critical strain indicating the elasticity of gel networks (c), 3D printing of Zn gel (d) and Cu gel (f) and their conversion into ZIF-8 (e) and HKUST-1 (g), three interval thixotropy test (3ITT) (h) of Zn and Cu gels and their shear rate sweep test (h, inset), and mechanical strength (i) and Young's modulus (j) of molded and 3D printed ZIF-8 and HKUST-1 objects.

shape is apparent in some ZIF-8 nanoparticles forming the skeletal network. Similarly, placing the copper precursor gel in 20 ml of 0.35 M TMA in ethanol/water (1 : 1) for 120 min at room temperature converts the gel into HKUST-1 with a marked color change (i.e., green to blue). The conversion follows pathway 2, and the crystallization of HKUST-1 alters the local structure but maintains pore interconnectivity, as shown in the SEM images.

The rheological properties of the Zn and Cu precursor gels are shown in Fig. 6h. The shear rate sweep test indicates the metal precursor gels display shear thinning behavior with a 2 kPa s decrease in viscosity under printing shear rates of 0.2 to 0.3 s^{-1}, enabling faster printing (up to 0.8 $mm^3 s^{-1}$). In addition, the metal precursor gels are viscoelastic according to the three-interval thixotropy test (3ITT), exhibiting a rapid (i.e., <1 s) rebound in viscosity (i.e., >1 kPa s) with the release of

shear stress allowing the printed gels to retain their extrusion shapes.

Ambient dried ZIF-8 and HKUST-1 objects, including molded cylinder ($d = 8.6$ mm, $h = 10.8$ mm), 3D-printed hollow cylinder (ID = 12 mm, OD = 14 mm, $h = 19$ mm), and 3D-printed 10-layer 90° rectangular grids yield improved strengths (Fig. 6i and j). Indeed, ZIF-8 and HKUST-1 cylinders (i.e., $d = 8.6$ mm, $h = 10.8$ mm) failed at 4.2 and 3.7% strain, respectively, corresponding to Young's moduli of 222.4 and 137.8 MPa. The 3D-printed 90° scaffolds fail at higher compressive deformations of 8.6% for ZIF-8 and 7.8% for HKUST, with Young's moduli of 217.3 and 152.7 MPa, respectively. The ZIF-8 and HKUST-1 hollow cylinders fail at 6.1% and 3.8% strains with the corresponding Young's moduli of 108.6 and 98.7 MPa, respectively. The lower failure strain and

poorer strength for the hollow cylinders is attributed to the creep deformation during gel printing causing sagging and irregular diameter resulting in an uneven force distribution over the structure during mechanical testing, while the 90° rectangular grid architecture provided better structural strength.

This work introduces a versatile technique for preparing complex 3D MOF objects and architectures that also allows manipulating the pores and structures of the material at the nanometer, micrometer, and millimeter scales. It begins with the preparation of formable and printable inorganic precursor alcogels from metal salts, followed by the infiltration of organic ligands to react and transform the gel network into crystallized MOFs. The gel strand diameter and network interconnectivity depend on the synthesis conditions,[86] and can be modified with additives, such as PAA. PAA addition also has the desired effect of changing the viscoelastic properties of the gel to allow for its direct printing *via* the extrusion process. Moreover, adding hard and soft templates can introduce ordered micro-, meso-, or micro-porosity to the final material.[87]

It is vital that the organic ligands can infiltrate and diffuse through the gel's interstitial liquids, and this work demonstrated that even bulky molecules could readily transport across the gel material. The gel liquid occupies 89.8% of the Zn precursor gel, and according to Fig. 2f, the liquid resides within interconnected pore channels having a mean diameter of 38 nm. However, it could be as large as 100 nm (Fig. 2k). It has been reported that following the macroscopic structural change during the sol-to-gel transition, molecules within the gel's liquid remain mobile,[88] with their transport rate dictated by their diffusion across liquid channels of complex shape and structure and by their interactions with the gel network. The measured diffusivity of inert molecules (*i.e.*, toluene and Sudan Red) in the gel was slower than in polystyrene gels,[89] but sufficient for this study.

During the reactive transformation of the gel network to MOFs, the gel liquid serves as the solvent and medium for the reaction and, therefore, must be carefully selected. The solvent exchange could be carried out to replace the gel liquid in the original alcogel to facilitate the reaction and transformation to MOFs (*e.g.*, methanol for ZIF-8, DMF for MOF-5, and a mixture of ethanol/water of 1 : 1 for HKUST-1). As the gel strands are thin (32 ± 7 nm), their complete dissolution must be avoided to prevent the collapse of the gel network. Nucleation is rapid due to the large surface area, and as the gel is thin, nucleation could occur both on its surface and in bulk. MOF, therefore, crystallizes and grows on the gel strand forming intergrown crystals (pathways 1 & 2). However, substantial gel dissolution can introduce dissolved metals, thus initiating nucleation and crystallization in the gel liquid, forming loose particles that assemble *via* percolation (pathway 3). Accordingly, a judicious control over the gel dissolution rate and MOF nucleation and crystallization rates can guide the transformation of precursor gel along the desired transformation pathway to obtain the target structure and porosity.

The gel-to-MOF transformation alters its skeletal network resulting in increased rigidity. Thus, it does not require

supercritical drying to preserve its pore structure and the materials can be dried under ambient conditions. Nevertheless, the MOF gel exhibits viscoelastic properties that can withstand significant external stresses and be further built upon and physically manipulated. Thus, using advanced 3D printing techniques, it is possible to prepare complex 3D objects from molecular to nano, micro, and millimeter length scales for various application demands such as catalysis,[90–92] separation,[93,94] and energy generation.[95,96] Moreover, this work demonstrated the versatility of this technique in preparing MOFs as illustrated in the twelve representative MOFs prepared in this work.

Conclusions

In summary, this work presents a versatile technique for preparing complex 3D MOF objects and architectures with a hierarchical network and pore structures by print extrusion of precursor gels and their controlled transformation into MOFs. The transformation process relies on the infiltration and diffusion of organic ligands, and their reactions with the gel network to initiate nucleation, crystallization, and growth of MOFs. Controlling the rates of gel dissolution, MOF nucleation, and crystal growth guides the transformation along different pathways from faithful replication of the original gel network (pathway 1) to a percolated assemblage of solution crystallized MOFs (pathway 3). After transformation, the MOF gel is viscoelastic and able to withstand external applied forces and retain its original printed shape. Thus, the prepared MOF 3D objects and architectures exhibit superb strength (>98.7 MPa), large open volume (1.1 cm^3 g^{-1}), and enormous surface area (*ca.* 1100 m^2 g^{-1}) with excellent gas permeability (>3.4 × 10^{-10} m^2) and diffusivity (≥5.8 × 10^{-6} m^2 s^{-1}).

Data availability

All experimental and computational data are available within the article or in the ESI file.†

Author contributions

K. L. Y., W. H., and Z. L. conceived the idea for the project and developed the methodology. Z. L. conducted the material synthesis and characterization. J. L. N. designed and built the 3D printer for metal precursor gels and assisted in 3D printing of the gel scaffolds. The FIB-SEM studies were done under the guidance of M. R. I. Z. L., W. H., and K. L. Y. conducted the data analyses and interpretation and wrote the original draft of the manuscript. K. L. Y., W. H., and J. K. C. K. supervised the research. All authors discussed and commented on the manuscript.

Conflicts of interest

Z. L., W. H., and K. L. Y. have a provisional patent application related to this work filed with the U.S. Patent and Trademark Office on 30 July 2021 (63227351).

Acknowledgements

Notes and references

1 S. Kitagawa, R. Kitaura and S. Noro, *Angew. Chem., Int. Ed.*, 2004, **43**, 2334–2375.

2 H. Furukawa, K. E. Cordova, M. O'Keeffe and O. M. Yaghi, *Science*, 2013, **341**, 1230444.

3 H. Li, M. Eddaoudi, M. O'Keeffe and O. M. Yaghi, *Nature*, 1999, **402**, 276–279.

4 O. Sato, *Nat. Chem.*, 2016, **8**, 644–656.

5 H. Deng, M. A. Olson, J. F. Stoddart and O. M. Yaghi, *Nat. Chem.*, 2010, **2**, 439–443.

6 F. X. Coudert, *Chem. Mater.*, 2015, **27**, 1905–1916.

7 A. Knebel, B. Geppert, K. Volgmann, D. Kolokolov, A. Stepanov, J. Twiefel, P. Heitjans, D. Volkmer and J. Caro, *Science*, 2017, **358**, 347–351.

8 D. Fairen-Jimenez, S. Moggach, M. Wharmby, P. Wright, S. Parsons and T. Duren, *J. Am. Chem. Soc.*, 2011, **133**, 8900–8902.

9 M. Tortora, P. Zajdel, A. R. Lowe, M. Chorążewski, J. B. Leão, G. V. Jensen, M. Bleuel, A. Giacomello, C. M. Casciola and S. Meloni, *Nano Lett.*, 2021, **21**, 2848–2853.

10 A. U. Ortiz, A. Boutin, A. H. Fuchs and F. X. Coudert, *Phys. Rev. Lett.*, 2012, **109**, 195502.

11 M. R. Ryder, B. Civalleri, G. Cinque and J. C. Tan, *CrystEngComm*, 2016, **18**, 4303–4312.

12 E. Jin, I. S. Lee, D. Kim, H. Lee, W. D. Jang, M. S. Lah, S. K. Min and W. Choe, *Sci. Adv.*, 2019, **5**, eaav4119.

13 M. Tchalala, P. Bhatt, K. Chappanda, S. Tavares, K. Adil, Y. Belmabkhout, A. Shkurenko, A. Cadiau, N. Heymans and G. De Weireld, *Nat. Commun.*, 2019, **10**, 1–10.

14 N. L. Rosi, J. Eckert, M. Eddaoudi, D. T. Vodak, J. Kim, M. O'Keeffe and O. M. Yaghi, *Science*, 2003, **300**, 1127–1129.

15 P. Horcajada, T. Chalati, C. Serre, B. Gillet, C. Sebrie, T. Baati, J. F. Eubank, D. Heurtaux, P. Clayette and C. Kreuz, *Nat. Mater.*, 2010, **9**, 172–178.

16 J. Lee, O. K. Farha, J. Roberts, K. A. Scheidt, S. T. Nguyen and J. T. Hupp, *Chem. Soc. Rev.*, 2009, **38**, 1450–1459.

17 M. Ding, R. W. Flaig, H. L. Jiang and O. M. Yaghi, *Chem. Soc. Rev.*, 2019, **48**, 2783–2828.

18 Y. Li, M. Karimi, Y.-N. Gong, N. Dai, V. Safarifard and H. L. Jiang, *Matter*, 2021, **4**, 2230–2265.

19 A. Corma, H. Garcia and F. Llabrés i Xamena, *Chem. Rev.*, 2010, **110**, 4606–4655.

20 M. D. Allendorf, A. Schwartzberg, V. Stavila and A. A. Talin, *Chem. Eur. J.*, 2011, **17**, 11372–11388.

21 P. Horcajada, R. Gref, T. Baati, P. K. Allan, G. Maurin, P. Couvreur, G. Ferey, R. E. Morris and C. Serre, *Chem. Rev.*, 2012, **112**, 1232–1268.

22 Q. Cheng, K. Tao, X. Han, Y. Yang, Z. Yang, Q. Ma and L. Han, *Dalton Trans.*, 2019, **48**, 4119–4123.

23 J. Xing, K. Guo, Z. Zou, M. Cai, J. Du and C. Xu, *Chem. Commun.*, 2018, **54**, 7046–7049.

24 J. Duan, S. Chen and C. Zhao, *Nat. Commun.*, 2017, **8**, 1–7.

25 O. Shekhah, L. Fu, R. Sougrat, Y. Belmabkhout, A. J. Cairns, E. P. Giannelis and M. Eddaoudi, *Chem. Commun.*, 2012, **48**, 11434–11436.

26 W. A. El-Mehalmey, A. H. Ibrahim, A. A. Abugable, M. H. Hassan, R. R. Haikal, S. G. Karakalos, O. Zaki and M. H. Alkordi, *J. Mater. Chem. A*, 2018, **6**, 2742–2751.

27 A. Sachse, R. Ameloot, B. Coq, F. Fajula, B. Coasne, D. De Vos and A. Galarneau, *Chem. Commun.*, 2012, **48**, 4749–4751.

28 P. Küsgens, A. Zgaverdea, H. G. Fritz, S. Siegle and S. Kaskel, *J. Am. Ceram. Soc.*, 2010, **93**, 2476–2479.

29 K. Huang, Z. Dong, Q. Li and W. Jin, *Chem. Commun.*, 2013, **49**, 10326–10328.

30 S. Zhou, X. Zou, F. Sun, F. Zhang, S. Fan, H. Zhao, T. Schiestel and G. Zhu, *J. Mater. Chem.*, 2012, **22**, 10322–10328.

31 Y. H. Cheung, K. Ma, M. C. Wasson, X. Wang, K. B. Idrees, T. Islamoglu, J. Mahle, G. W. Peterson, J. H. Xin and O. K. Farha, *Angew. Chem., Int. Ed.*, 2022, **61**, e202202207.

32 X. Dong, M. Cui, R. Huang, R. Su, W. Qi and Z. J. L. He, *Langmuir*, 2020, **36**, 1212–1220.

33 L. Zhu, L. Zong, X. Wu, M. Li, H. Wang, J. You and C. Li, *ACS Nano*, 2018, **12**, 4462–4468.

34 Y. Chen, F. Chen, S. Zhang, Y. Cai, S. Cao, S. Li, W. Zhao, S. Yuan, X. Feng, A. Cao, X. Ma and B. Wang, *J. Am. Chem. Soc.*, 2017, **139**, 16482–16485.

35 H. Zhu, X. Yang, E. D. Cranston and S. Zhu, *Adv. Mater.*, 2016, **28**, 7652–7657.

36 N. Huang, H. Drake, J. Li, J. Pang, Y. Wang, S. Yuan, Q. Wang, P. Cai, J. Qin and H. C. Zhou, *Angew. Chem. Int. Ed.*, 2018, **130**, 9054–9058.

37 H. Zhang, W. Zhao, M. Zou, Y. Wang, Y. Chen, L. Xu, H. Wu and A. Cao, *Adv. Energy Mater.*, 2018, **8**, 1800013.

38 H. Zhao, Y. Chen, Q. Peng, Q. Wang and G. Zhao, *Appl. Catal., B*, 2017, **203**, 127–137.

39 W. Liang, B. Wang, J. Cheng, D. Xiao, Z. Xie and J. Zhao, *J. Hazard. Mater.*, 2021, **401**, 123718.

40 J. Gu, H. Fan, C. Li, J. Caro and H. Meng, *Angew. Chem.*, 2019, **131**, 5351–5355.

41 J. Mao, M. Ge, J. Huang, Y. Lai, C. Lin, K. Zhang, K. Meng and Y. Tang, *J. Mater. Chem.*, 2017, **5**, 11873–11881.

42 J. Mao, Y. Tang, Y. Wang, J. Huang, X. Dong, Z. Chen and Y. J. I. Lai, *iScience*, 2019, **16**, 133–144.

43 W. Xia, C. Qu, Z. Liang, B. Zhao, S. Dai, B. Qiu, Y. Jiao, Q. Zhang, X. Huang, W. Guo, D. Dang, R. Zou, D. Xia, Q. Xu and M. Liu, *Nano Lett.*, 2017, **17**, 2788–2795.

44 Y. Chen, X. Huang, S. Zhang, S. Li, S. Cao, X. Pei, J. Zhou, X. Feng and B. Wang, *J. Am. Chem. Soc.*, 2016, **138**, 10810–10813.

45 B. M. Connolly, M. Aragones-Anglada, J. Gandara-Loe, N. A. Danaf, D. C. Lamb, J. P. Mehta, D. Vulpe, S. Wuttke, J. Silvestre-Albero and P. Z. Moghadam, *Nat. Commun.*, 2019, **10**, 1–11.

46 A. Ahmed, M. Forster, R. Clowes, P. Myers and H. Zhang, *Chem. Commun.*, 2014, **50**, 14314–14316.

47 B. M. Connolly, D. G. Madden, A. E. Wheatley and D. Fairen-Jimenez, *J. Am. Chem. Soc.*, 2020, **142**, 8541–8549.

48 T. Tian, Z. Zeng, D. Vulpe, M. E. Casco, G. Divitini, P. A. Midgley, J. Silvestre-Albero, J. C. Tan, P. Z. Moghadam and D. Fairen-Jimenez, *Nat. Mater.*, 2018, **17**, 174–179.

49 B. Bueken, N. Van Velthoven, T. Willhammar, T. Stassin, I. Stassen, D. A. Keen, G. V. Baron, J. F. Denayer, R. Ameloot and S. Bals, *Chem. Sci.*, 2017, **8**, 3939–3948.

50 M. R. Lohe, M. Rose and S. Kaskel, *Chem. Commun.*, 2009, 6056–6058.

51 L. Li, S. Xiang, S. Cao, J. Zhang, G. Ouyang, L. Chen and C. Y. Su, *Nat. Commun.*, 2013, **4**, 1–9.

52 M. O. M. Piepenbrock, G. O. Lloyd, N. Clarke and J. W. Steed, *Chem. Rev.*, 2010, **110**, 1960–2004.

53 M. Kalaj, K. C. Bentz, S. Ayala Jr, J. M. Palomba, K. S. Barcus, Y. Katayama and S. M. Cohen, *Chem. Rev.*, 2020, **120**, 8267–8302.

54 S. Schmitt, S. Diring, P. G. Weidler, S. Begum, S. Heißler, S. Kitagawa, C. Wöll, S. Furukawa and M. Tsotsalas, *Chem. Mater.*, 2017, **29**, 5982–5989.

55 T. Tian, J. Velazquez-Garcia, T. D. Bennett and D. Fairen-Jimenez, *J. Mater. Chem. A*, 2015, **3**, 2999–3005.

56 S. Lawson, A. A. Alwakwak, A. A. Rownaghi and F. Rezaei, *ACS Appl. Mater. Interfaces*, 2020, **12**(50), 56108–56117.

57 G. Cai, P. Yan, L. Zhang, H. C. Zhou and H. L. Jiang, *Chem. Rev.*, 2021, **121**, 12278–12326.

58 N. Huang, H. Drake, J. Li, J. Pang, Y. Wang, S. Yuan, Q. Wang, P. Cai, J. Qin and H. C. Zhou, *Angew. Chem., Int. Ed.*, 2018, **57**, 8916–8920.

59 Y. Yao, C. Wang, J. Na, M. S. A. Hossain, X. Yan, H. Zhang, M. A. Amin, J. Qi, Y. Yamauchi and J. Li, *Small*, 2022, **18**, 2104387.

60 P. Cheng, M. Kim, H. Lim, J. Lin, N. L. Torad, X. Zhang, M. S. A. Hossain, C. W. Wu, C. Wang, J. Na and Y. Yamauchi, *Adv. Sustainable Syst.*, 2020, **4**, 2000060.

61 W. Ren, J. Gao, C. Lei, Y. Xie, Y. Cai, Q. Ni and J. Yao, *Chem. Eng. J.*, 2018, **349**, 766–774.

62 G. A. Stenmark, *Anal. Chem.*, 1957, **29**, 1367–1369.

63 J. Livage, M. Henry and C. Sanchez, *Prog. Solid State Chem.*, 1988, **18**, 259–341.

64 A. E. Gash, T. M. Tillotson, J. H. Satcher Jr, L. W. Hrubesh and R. L. Simpson, *J. Non-Cryst. Solids*, 2001, **285**, 22–28.

65 P. J. Lu, E. Zaccarelli, F. Ciulla, A. B. Schofield, F. Sciortino and D. A. J. N. Weitz, *Nature*, 2008, **453**, 499–503.

66 X. Lu, G. Hasegawa, K. Kanamori and K. Nakanishi, *J. Sol-Gel Sci. Technol.*, 2020, **95**, 530–550.

67 P. J. Lu, E. Zaccarelli, F. Ciulla, A. B. Schofield, F. Sciortino and D. A. Weitz, *Nature*, 2008, **453**, 499–503.

68 Y. Hu, H. Kazemian, S. Rohani, Y. Huang and Y. Song, *Chem. Commun.*, 2011, **47**, 12694–12696.

69 S. Bordiga, J. G. Vitillo, G. Ricchiardi, L. Regli, D. Cocina, A. Zecchina, B. Arstad, M. Bjørgen, J. Hafizovic and K. P. Lillerud, *J. Am. Chem. Soc.*, 2005, **109**, 18237–18242.

70 D. Stoeckel, C. Kübel, K. Hormann, A. Höltzel, B. M. Smarsly and U. Tallarek, *Langmuir*, 2014, **30**, 9022–9027.

71 A. Katti, N. Shimpi, S. Roy, H. Lu, E. F. Fabrizio, A. Dass, L. A. Capadona and N. Leventis, *Chem. Mater.*, 2006, **18**, 285–296.

72 M. A. B. Meador, E. F. Fabrizio, F. Ilhan, A. Dass, G. Zhang, P. Vassilaras, J. C. Johnston and N. Leventis, *Chem. Mater.*, 2005, **17**, 1085–1098.

73 M. Koebel, A. Rigacci and P. Achard, *J. Sol-Gel Sci. Technol.*, 2012, **63**, 315–339.

74 K. S. Park, Z. Ni, A. P. Côté, J. Y. Choi, R. Huang, F. J. Uribe-Romo, H. K. Chae, M. O'Keeffe and O. M. Yaghi, *Proc. Natl. Acad. Sci.*, 2006, **103**, 10186–10191.

75 C. S. Tsao, M. S. Yu, T. Y. Chung, H. C. Wu, C. Y. Wang, K. S. Chang and H. L. Chen, *J. Am. Chem. Soc.*, 2007, **129**, 15997–16004.

76 Y. Pan, Y. Liu, G. Zeng, L. Zhao and Z. Lai, *Chem. Commun.*, 2011, **47**, 2071–2073.

77 J. Hafizovic, M. Bjørgen, U. Olsbye, P. D. Dietzel, S. Bordiga, C. Prestipino, C. Lamberti and K. P. Lillerud, *J. Am. Chem. Soc.*, 2007, **129**, 3612–3620.

78 C. J. Geankoplis, A. A. Hersel and D. H. Lepek, *Transport Processes and Separation Process Principles*, Prentice Hall, Boston, MA, USA, 2018.

79 X. Zhao, S. Wang, X. Yin, J. Yu and B. Ding, *Sci. Rep.*, 2016, **6**, 1–11.

80 W. K. Kim, E. A. Payzant, S. Yoon and T. J. Anderson, *J. Cryst. Growth*, 2006, **294**, 231–235.

81 F. Millange, R. El Osta, M. E. Medina and R. I. Walton, *CrystEngComm*, 2011, **13**, 103–108.

82 J. Cravillon, C. A. Schröder, H. Bux, A. Rothkirch, J. Caro and M. Wiebcke, *CrystEngComm*, 2012, **14**, 492–498.

83 E. Ruiz-Agudo, C. Putnis and A. Putnis, *Chem. Geol.*, 2014, **383**, 132–146.

84 R. Hellmann, S. Cotte, E. Cadel, S. Malladi, L. S. Karlsson, S. Lozano-Perez, M. Cabié and A. Seyeux, *Nat. Mater.*, 2015, **14**, 307–311.

85 F. Xia, J. Brugger, Y. Ngothai, B. O'Neill, G. Chen and A. Pring, *Cryst. Growth Des.*, 2009, **9**, 4902–4906.

86 C. Ziegler, A. Wolf, W. Liu, A. K. Herrmann, N. Gaponik and A. Eychmüller, *Angew. Chem., Int. Ed.*, 2017, **56**, 13200–13221.

87 N. D. Petkovich and A. Stein, *Chem. Soc. Rev.*, 2013, **42**, 3721–3739.

88 B. Dunn and J. I. Zink, *Chem. Mater.*, 1997, **9**, 2280–2291.

89 W. T. Ford, B. J. Ackerson, F. D. Blum, M. Periyasamy and S. Pickup, *J. Am. Chem. Soc.*, 1987, **109**, 7276–7280.

90 Q. Wang, Z. Li, M. A. Banares, L. T. Weng, Q. Gu, J. Price, W. Han and K. L. Yeung, *Small*, 2019, **15**, 1903525.

91 Y. Li, W. Han, R. Wang, L. T. Weng, A. Serrano-Lotina, M. A. Banares, Q. Wang and K. L. Yeung, *Appl. Catal., B*, 2020, **275**, 119121.

92 Q. Wang, Y. Li, A. Serrano-Lotina, W. Han, R. Portela, R. X. Wang, M. A. Banares and K. L. Yeung, *J. Am. Chem. Soc.*, 2021, **143**, 196–205.

93 V. C. Ramos, W. Han and K. L. Yeung, *Environ. Res.*, 2022, **215**, 114341.

94 V. C. Ramos, W. Han, X. Zhang, S. Zhang and K. L. Yeung, *Environ. Res.*, 2023, **219**, 115000.

95 K. He, W. Han and K. L. Yeung, *J. Taiwan Inst. Chem. Eng.*, 2019, **98**, 85–93.

96 R. Deng, W. Han and K. L. Yeung, *Catal. Today*, 2019, **331**, 12–17.